This CVPR 2021 paper is the Open Access version, provided by the Computer Vision Foundation.
Except for this watermark, it is identical to the accepted version;
the final published version of the proceedings is available on IEEE Xplore.

Shape from Sky: Polarimetric Normal Recovery Under The Sky

Tomoki Ichikawa[†*] Matthew Purri[‡*] Ryo Kawahara[†] Shohei Nobuhara[†] Kristin Dana[‡] Ko Nishino[†]
† Kyoto University
https://vision.ist.i.kyoto-u.ac.jp/
‡ Rutgers University
https://www.ece.rutgers.edu/~kdana/

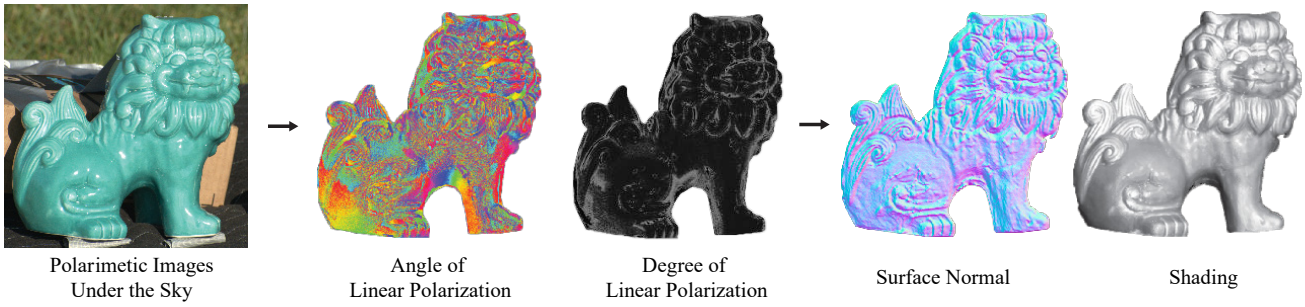

Figure 1: We introduce a novel method for reconstructing fine geometry of non-Lambertian objects from passive observations under the sky. The method fully leverages the polarimetric properties of sky and sun light encoded in the reflection by the surface to recover the surface normal at each pixel.

Abstract

The sky exhibits a unique spatial polarization pattern by scattering the unpolarized sun light. Just like insects use this unique angular pattern to navigate, we use it to map pixels to directions on the sky. That is, we show that the unique polarization pattern encoded in the polarimetric appearance of an object captured under the sky can be decoded to reveal the surface normal at each pixel. We derive a polarimetric reflection model of a diffuse plus mirror surface lit by the sun and a clear sky. This model is used to recover the per-pixel surface normal of an object from a single polarimetric image or from multiple polarimetric images captured under the sky at different times of the day. We experimentally evaluate the accuracy of our shape-from-sky method on a number of real objects of different surface compositions. The results clearly show that this passive approach to fine-geometry recovery that fully leverages the unique illumination made by nature is a viable option for 3D sensing. With the advent of quad-Bayer polarization chips, we believe the implications of our method span a wide range of domains.

1. Introduction

Methods for 3D reconstruction have been of central interest in computer vision since its inception. A robust solution to it underlies a wide range of applications within vision and in surrounding areas including robotics, extended reality (XR), and medicine. The challenge of this 2D to 3D inverse problem lies in the combination surface reflectance and incident illumination that generates the complex appearance of a given geometry.

In this work, we are interested in recovering the fine geometry represented by per-pixel surface normals. Surface normal recovery can be interpreted as decoding the incident illumination from its reflectance-modulated pixel intensity. If we know the spatial pattern of the illumination (*e.g.*, three point sources) and the reflectance dictated by the object material properties (*e.g.*, Lambertian), we can "demodulate" the pixel intensity to obtain the surface normal.

Consider two simple models of the interaction of light at a surface. On one hand, the appearance of a Lambertian surface lit by a point source can be perfectly modeled with simple linear equations from which we can recover per-pixel surface normals. On the other hand, the appearance of an ideal mirror surface captured under a rainbow-like angularly unique illumination directly tells us per-pixel surface normals by simple lookup.

The reality, however, lives somewhere in between a set of simple point source illumination and an angularly unique one, and we generally do not know the exact reflectance. As a result, we are forced to solve an ill-posed problem blindly. This has led to numerous methods in the space such as pho-

∗ Equal contribution.

tometric stereo of objects with reflectance of varying complexity and inverse rendering with strong statistical priors.

Is there any real-world situation in which we can assume a known illumination pattern that is sufficiently unique across its spatial or angular span? If so, we could reduce this disentanglement problem to decoding the unknown modulation by the reflection while simultaneously recovering the surface normal. Is there such a unique imaging setup that is readily accessible, and how can we fully leverage it to recover fine geometry, namely per-pixel surface normals of arbitrary material objects?

In this paper, we show that indeed there exists a very convenient lighting setup right above us: the sky. The sky, on a clear day, has an angular polarization distribution uniquely defined by the latitude and longitude centered around the sun. The Rayleigh sky model conveniently predicts both the angle of polarization (AOP) and the degree of polarization (DOP) across the sky as illustrated in Figure 2 [28]. We show that this everyday, but special angular polarization pattern readily gives us sufficient incident cues that are modulated by the unknown reflectance and unknown surface normals so that we can robustly decode it to recover spatially varying reflectance and per-pixel surface normals.

We conduct a number of experiments using real images taken outdoors with a linear polarizer at the camera or with a quad-Bayer polarization camera. The results clearly demonstrate that our method can recover accurate fine geometry of objects with complex reflectance from a single or a few polarimetric images taken completely passively. The implication of this work is far-reaching. With the advent of polarization cameras using quad-sensor chips, the proposed work gives the ability to perform 3D reconstruction under natural lighting without point matching. Furthermore, while specular surfaces are typically challenging to reconstruct with geometric methods, these surfaces are particularly well-suited for shape-from-sky.

2. Related Work

As light interacts with a surface, its polarization state is altered. The light is transformed depending on surface properties including local geometry and material type. This effect has been modeled and utilized in Shape-from-Polarization (SfP) to estimate the geometry of a surface. Early works constrain the problem by estimating the geometry of only dielectric materials and assume a solely diffuse reflection polarization model [1, 18, 20]. Other works use polarization characteristics of specular reflection to reconstruct specular surfaces such as metallic objects [19, 23].

Realistically, light is reflected off of a material surface as a mixture of diffuse and specular reflections. As such, methods that utilize a mixed diffuse and specular model generate more faithful representations of objects [16, 24, 26, 29]. These methods include both reflectance types into their models by imaging the object at specific orientations in order to capture a diffuse polarized image or by classifying each pixel as diffuse or specular dominant. Riviere *et al*. separate the specular component of the reflected light by imaging the planar surface several times near the Brewster angle of incidence [24]. It is unclear how to extend this imaging procedure to objects with less planar structures. Baek *et al*. develop a complete pBRDF model that can model both diffuse and specular polarized reflections from a single projector and camera setup [2]. Other methods [6, 8] use polarized color gradient illumination for surface normal estimation.

In many previous works, SfP is computed on objects in possibly unknown but controlled illumination environments. Smith *et al*. reconstruct 3D geometries of objects outside of a controlled setting by estimating the illumination source as a point source with 1st or 2nd order spherical harmonics [26]. Similar methods alternatively optimize the surface geometry and illumination orientation to resolve the Bas-relief ambiguity [25]. SfP is often combined with methods such as Shape-from-Shading or photometric stereo in order to resolve the ambiguity but require additional imaging devices or procedures [15, 20, 30, 34]. Zhu *et al*. require an RGB stereo pair for 3D estimation [34] while Ngo *et al*. require several illumination views at sufficiently large distances [20]. SfP combined with multi-view stereo requires polarimetric images from multiple viewpoints [4, 33]. Prior work that estimates surface normals in uncontrolled outdoor illumination [10] assumes a simple model of an unpolarized overcast sky.

In contrast, we take advantage of the polarization of skylight and its hemispherical pattern that can be expressed by the Rayleigh sky model [9, 27]. This distinct sky polarization pattern is important to insects and animals for navigation [12, 13, 17, 31, 32]; and for recognizing bodies of water via sky reflections [7, 14]. In this work, we show that the angular variation of polarization under the blue sky is a key for surface normal estimation. Analogous to the use of multiple polarized sources in polarization multiplexing for reflectance estimation [5, 6], the sky provides a hemisphere of distinctly polarized sources. We use a mixed polarization reflectance model (diffuse and specular) with a monocular polarized camera setup to reconstruct the geometry of an object under uncontrolled natural illumination.

3. Linear Polarization and Reflection

Let us first review basic properties of light polarization and how it is modulated by surface reflection including mirror and diffuse reflection. We then review how we can model polarization of sky light. Table 1 summarizes primary notations.

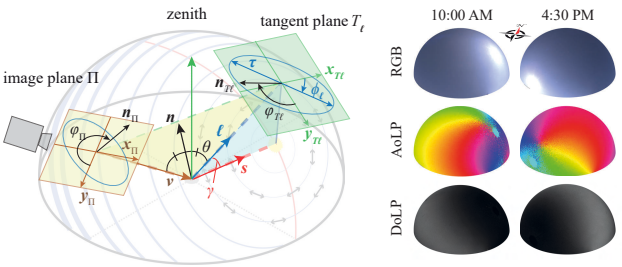

Figure 2: The polarization pattern and geometry of sky reflection. **Left.** The angle of polarization of the sky, depicted with double-sided arrows is constant along great circles passing the sun (longitudes). The degree of polarization is constant on the small circles perpendicular to the solar direction (latitudes), where different thicknesses indicate their magnitudes. Nomenclature is defined in Table 1. **Right.** The hemispheres are real images captured at two times of a day by the on-chip polarizer camera with a fisheye lens. Our proposed method makes use of the unique and often overlooked polarization pattern of the sky.

3.1. Polarization

Light as an electromagnetic field propagates as a collection of plane waves whose orientations can be defined on the plane perpendicular to the direction of propagation [3, 11]. For unpolarized light, these plane waves are randomly oriented. However, for linearly polarized light, they are aligned in one direction. Light is often composed of various magnitudes of such linearly polarized light of different orientations. We call such light partially (linearly) polarized. When viewed on the plane perpendicular to the traverse direction, these plane waves carve out an ellipse which can be collectively expressed with a single cosine wave in the angular domain ν

$$I(\nu) = I + \rho I \cos\left(2\nu - 2\phi\right), \tag{1}$$

where I is the radiance of the light, ρ is the degree of polarization (DoP), and ϕ is the angle of polarization (AoP). Light can also be circularly polarized in which case the plane-of-vibration rotates with a unique period. In this paper, we only consider linear polarization, as regular surface reflection primarily only causes linear polarization. In this case, linearly polarized light can also be conveniently expressed with the first three entries of the Stokes vector as

$$\mathsf{S} = \begin{bmatrix} 2I \\ 2\rho I \cos 2\phi \\ 2\rho I \sin 2\phi \\ 0 \end{bmatrix}. \tag{2}$$

$\boldsymbol{v}$	viewing direction
$\boldsymbol{n}(\boldsymbol{x})$	surface normal corresponding to pixel $\boldsymbol{x}$
$\boldsymbol{s}$	sun direction
$\boldsymbol{\ell}(\boldsymbol{x})$	directional vector to the sky in mirror direction from pixel $\boldsymbol{x}$ $\left(\boldsymbol{\ell}(\boldsymbol{x}) = \boldsymbol{v} - 2\left(\boldsymbol{v}^\mathsf{T}\boldsymbol{n}(\boldsymbol{x})\right)\boldsymbol{n}(\boldsymbol{x})\right)$
γ	angle between $\boldsymbol{\ell}$ and $\boldsymbol{s}$
$\boldsymbol{\theta}$	angular coordinate of incident and exitant light (*e.g.*, $\boldsymbol{\theta}_i = (\theta_i, \varphi_i)$)
$T_{\boldsymbol{\ell}}$	tangent plane of sky at $\boldsymbol{\ell}$, whose up vector $\boldsymbol{y}_{T_{\boldsymbol{\ell}}}$ points opposite to the camera's up vector
$\boldsymbol{n}_{T_{\boldsymbol{\ell}}}$	normalized projection of $\boldsymbol{n}$ onto the tangent plane at $\boldsymbol{\ell}$
$\varphi_{T_{\boldsymbol{\ell}}}$	angle the projected normal makes with the up vector of tangent plane $(\cos^{-1} \boldsymbol{n}_{T_{\boldsymbol{\ell}}} \cdot \boldsymbol{y}_{T_{\boldsymbol{\ell}}})$ [1]
$\phi_{\boldsymbol{\ell}}$	angle of polarization of sky at $\boldsymbol{\ell}$ $(\boldsymbol{\ell} \times \boldsymbol{s})$ from Rayleigh sky model
$\boldsymbol{n}_\Pi$	normalized projection of $\boldsymbol{n}$ onto image plane Π
φ_Π	angle the image projected normal $(\boldsymbol{n}_\Pi)$ makes with the up vector of image plane $(\boldsymbol{y}_\Pi)$

Table 1: Nomenclature

3.2. Polarimetric Reflection

The linear polarization and intensity of an incident polarized light S_i to a surface is modulated by reflection before observed as exitant polarized light S_o. This modulation can be expressed with a Mueller matrix $\boldsymbol{M}$

$$\mathsf{S}_o = \boldsymbol{M}\mathsf{S}_i. \tag{3}$$

Equation 3 provides relationship between the known Stokes vectors of the sky (from the Rayleigh sky model) to the observed Stokes vectors at the camera (observable using a rotating polarizer at the camera or by using a quad-Bayer polarization camera) via the Mueller matrix with the local surface normal as the primary surface parameter that we seek to recover.

For a mirror reflection the Mueller matrix can be expressed with a series of transformations

$$\boldsymbol{M} = k\boldsymbol{C}(\varphi_o)\boldsymbol{R}(\theta)\boldsymbol{C}(-\varphi_i), \tag{4}$$

where k denotes a scalar coefficient depending on the normal $\boldsymbol{n}$, $\boldsymbol{C}$ is a rotation matrix

$$\boldsymbol{C}(\varphi) = \begin{bmatrix} 1 & 0 & 0 & 0 \\ 0 & \cos(2\varphi) & -\sin(2\varphi) & 0 \\ 0 & \sin(2\varphi) & \cos(2\varphi) & 0 \\ 0 & 0 & 0 & 1 \end{bmatrix}, \tag{5}$$

and $\boldsymbol{R}$ denotes polarization transformation by reflection. The light is first rotated into the incident plane coordinate

[1] This is abbreviated from $\phi_{\boldsymbol{n}_{T_{\boldsymbol{\ell}}}}$.

frame with $\boldsymbol{C}(-\varphi_i)$ where φ_i is the angle between the plane of incident light and the y-axis of the coordinate frame in which the incident light is defined. After reflection expressed by $\boldsymbol{R}$, the polarization state is coordinate transformed into the outgoing (viewing) direction φ_o.

The polarization transform by reflection $\boldsymbol{R}$ can consist of different components. A full polarization BRDF model has been derived in [2]. In this paper, we assume the material surface of interest exhibits a linear combination of specular (mirror) and diffuse reflection.

Specular Reflection Polarization transform by specular reflection can be fully expressed with Fresnel equations

$$\boldsymbol{R}(\theta) = \begin{bmatrix} R_+ & R_- & 0 & 0 \\ R_- & R_+ & 0 & 0 \\ 0 & 0 & R_\times \cos\delta & 0 \\ 0 & 0 & 0 & R_\times \cos\delta \end{bmatrix}, \tag{6}$$

where $R_\pm = \frac{R_s \pm R_p}{2}$, $R_\times = \sqrt{R_p R_s}$, θ is the incident angle of the light, and $\cos\delta$ is -1 when θ is less than Brewster's angle and 1 otherwise. R_s and R_p are the Fresnel coefficients defined as

$$R_s(\theta) = \left(\frac{\sin(\theta-\theta_t)}{\sin(\theta+\theta_t)}\right)^2, \quad R_p(\theta) = \left(\frac{\tan(\theta-\theta_t)}{\tan(\theta+\theta_t)}\right)^2, \tag{7}$$

respectively. Here θ_t is given by Snell's law as

$$\theta_t = \sin^{-1}\left(\frac{\mu_a}{\mu_m}\sin\theta\right), \tag{8}$$

where μ_a and μ_m denote the indices of refraction of air and the object material, respectively.

Diffuse reflection Diffuse reflection is slightly more involved as the polarized light enters the object surface, gets depolarized by scattering, but then becomes polarized again when exiting from the interface to air. Assuming Lambertian reflection, the diffuse reflection observed by a viewer for an infinitesimally small solid angle of an incident polarized light S_i is

$$d\mathsf{S}_o = \frac{\boldsymbol{n}\cdot\boldsymbol{\ell}}{2\pi}\boldsymbol{C}(\varphi_o)\boldsymbol{T}(\theta_o)\boldsymbol{D}(\zeta)\boldsymbol{T}(\theta_i)\boldsymbol{C}(-\varphi_i)\mathsf{S}_i d\omega, \tag{9}$$

where θ_o denotes the transmittance angle from the interior of the object surface to the viewer given as $\theta_o = \sin^{-1}\left(\frac{\mu_a}{\mu_m}\sin\theta\right)$, ζ is the diffuse albedo, $\boldsymbol{n}$ is the surface normal, and $\boldsymbol{\ell}$ is the direction of the incoming light (direction to a sky patch is used for example). $\boldsymbol{D}(\zeta)$ is the 4×4 depolarization matrix

$$\boldsymbol{D}(\zeta) = \begin{bmatrix} \zeta & 0 & 0 & 0 \\ 0 & 0 & 0 & 0 \\ 0 & 0 & 0 & 0 \\ 0 & 0 & 0 & 0 \end{bmatrix}. \tag{10}$$

The polarization transform by transmission when entering and exiting the interface is

$$\boldsymbol{T}(\theta) = \begin{bmatrix} T_+ & T_- & 0 & 0 \\ T_- & T_+ & 0 & 0 \\ 0 & 0 & T_\times & 0 \\ 0 & 0 & 0 & T_\times \end{bmatrix}, \tag{11}$$

where $T_\pm = \frac{T_s \pm T_p}{2}$, $T_\times = \sqrt{T_p T_s}$ and θ is the incident angle of the light. T_s and T_p are the Fresnel coefficients defined as

$$T_s(\theta) = 1 - R_s(\theta), \quad T_p(\theta) = 1 - R_p(\theta), \tag{12}$$

respectively.

The total irradiance of diffuse reflection to the observer (*e.g.*, camera) is the integration of this differential polarized light (Eq. 9) over the upper hemisphere Ω of incident light around the surface normal

$$\mathsf{S}_o = \frac{1}{2\pi}\boldsymbol{C}(\varphi_o)\boldsymbol{T}(\theta_o)\int_\Omega (\boldsymbol{n}\cdot\boldsymbol{\ell})\boldsymbol{D}(\zeta)\boldsymbol{T}(\theta_i)\boldsymbol{C}(-\varphi_i)\mathsf{S}_i d\omega. \tag{13}$$

4. Sky Polarization

As depicted in Fig. 2, the sky exhibits a unique pattern of linear polarization. When observing an object surface captured on a clear day sky with a polarization camera, we are essentially observing this sky polarization pattern modulated by the surface reflection and geometry.

Sky Polarization Distribution The sky can be geometrically modeled as a directional light distribution over the upper hemisphere with its zenith aligned with the surface normal of the ground. Let us denote the sun direction with $\boldsymbol{s}$. While the sun is unpolarized, Rayleigh showed that Rayleigh scattering of sun light induces unique symmetry in its polarization over the sky [28].

The angle of polarization form iso-contours (great circles, meridians) passing through the sun (*i.e.*, in longitude). That is, the polarization direction on the tangent plane $T_{\boldsymbol{\ell}}$ is $\boldsymbol{\ell}\times\boldsymbol{s}$. We consider a right-hand coordinate frame with the z-direction pointing towards the viewing direction.

As depicted in Fig. 2, the camera coordinate frame in the tangent plane coordinates becomes

$$\boldsymbol{C}_{T_{\boldsymbol{\ell}}} = \begin{bmatrix} \frac{\boldsymbol{\ell}\times[0\ -1\ 0]}{\|\boldsymbol{\ell}\times[0\ -1\ 0]\|} \end{bmatrix}^\mathsf{T} \quad \boldsymbol{\ell}\times\boldsymbol{x}_{T_{\boldsymbol{\ell}}} \quad \boldsymbol{\ell} \end{bmatrix}^\mathsf{T}. \tag{14}$$

The sky polarization direction in the tangent plane coordinate frame then becomes

$$\boldsymbol{\tau} = \boldsymbol{C}_{T_{\boldsymbol{\ell}}}\boldsymbol{\ell}\times\boldsymbol{s}, \tag{15}$$

and the observed angle of sky polarization is

$$\phi_{\boldsymbol{\ell}} = \tan^{-1}(\boldsymbol{\tau}_y/\boldsymbol{\tau}_x). \tag{16}$$

The degree of polarization of the sky $\rho_{\boldsymbol{\ell}}$, in contrast, form iso-contours (parallels) around the sun (*i.e.*, in latitude)

$$\rho_{\boldsymbol{\ell}} = \rho_{\max} \frac{\sin^2 \gamma}{1 + \cos^2 \gamma}\,, \tag{17}$$

where $\rho_{\max}$ is an unknown scaling factor[2] and $\gamma = \cos^{-1} \boldsymbol{\ell}^{\mathsf{T}} \boldsymbol{s}$.

Sky Intensity Distribution In addition to the polarization characteristics, we must also take into account the radiance distribution of the sky. The Perez sky model [22] expresses the sky intensity distribution relative to a sampled reference intensity at a known direction. Let us denote the zenith vector of the sky in the camera coordinate frame with $\boldsymbol{g}$. The sky intensity of the direction $\boldsymbol{\ell}(\boldsymbol{x})$ is then given by

$$I_{\boldsymbol{\ell}(\boldsymbol{x})} = \frac{f(\boldsymbol{g}, \boldsymbol{s}, \boldsymbol{\ell}(\boldsymbol{x}))}{f(\boldsymbol{g}, \boldsymbol{s}, \boldsymbol{\ell}(\boldsymbol{x}_0))} I_{\boldsymbol{\ell}(\boldsymbol{x}_0)}\,, \tag{18}$$

where

$$f = \left(1 + a \exp\left(b/(\boldsymbol{g}^{\top}\boldsymbol{\ell})\right)\right)\left(1 + c \exp\left(d\gamma\right) + e(\boldsymbol{s}^{\top}\boldsymbol{\ell})^2\right)\,. \tag{19}$$

The values of the coefficients a, b, c, d and e depend on the conditions of sky.

5. Polarimetric Shape from Sky

We are now ready to derive a method for recovering the surface normals of an object whose polarimetric image is captured under the sky. Regardless of the image capturing setup (*e.g.*, rotated filter, quad-Bayer polarization camera, *etc.*), we show that polarimetric observations at each pixel can be turned into surface normals.

We make a few moderate assumptions about the target surface and the imaging setup. We assume that the surface reflection consists of a linear combination of Lambertian diffuse reflection and perfect mirror reflection. This does limit the applicability of our method to specular objects. We leave extensions to glossy surfaces as our future work. We assume that the camera model can be approximated with orthographic projection and that the polarimetric images are taken under a clear sky. Clouds attenuate the sky polarization affecting the degree of polarization in addition to the spatial intensity pattern. We plan to extend our method to non-clear skies in our future work.

5.1. Polarimetric Sky Reflection

Let us first derive a generative model of the forward imaging process of the sky polarization via object surface reflection. For this, we denote the surface normal of the object surface captured at image coordinates $\boldsymbol{x}$ with $\boldsymbol{n}(\boldsymbol{x})$, which we recover in the 3D camera coordinate frame.

[2]It is set to 1.0 in textbooks in general.

We assume orthographic projection. The angle this surface normal makes with the y-axis of the image plane is

$$\varphi_{\Pi}(\boldsymbol{x}) = \cos^{-1}(\boldsymbol{n}_{\Pi}(\boldsymbol{x})^{\mathsf{T}}\, \boldsymbol{y}_{\Pi})\,. \tag{20}$$

The sky direction in perfect mirror direction to the orthographic viewing direction by this surface normal is

$$\boldsymbol{\ell}(\boldsymbol{x}) = \boldsymbol{v} - 2\left(\boldsymbol{v}^{\top}\boldsymbol{n}(\boldsymbol{x})\right)\boldsymbol{n}\,. \tag{21}$$

For any sky direction, we can compute its Stokes vector $\mathsf{S}_{\boldsymbol{\ell}(\boldsymbol{x})}$ from its intensity, angle, and degree of polarization, Eq. 19, Eq. 16 and Eq. 17, respectively,

$$\mathsf{S}_{\boldsymbol{\ell}(\boldsymbol{x})} = 2 I_{\boldsymbol{\ell}(\boldsymbol{x})} \begin{bmatrix} 1 \\ \rho_{\boldsymbol{\ell}} \cos 2\phi_{\boldsymbol{\ell}} \\ \rho_{\boldsymbol{\ell}} \sin 2\phi_{\boldsymbol{\ell}} \\ 0 \end{bmatrix}\,. \tag{22}$$

This Stokes vector $\mathsf{S}_{\boldsymbol{\ell}(\boldsymbol{x})}$ is transformed into the observed Stokes vector $\mathsf{S}_{\boldsymbol{x}}$ by surface reflection. For the coordinate transforms between the incident sky light tangent plane $T_{\boldsymbol{\ell}}$ and the plane of reflection, as well as that between the plane of reflection and the camera coordinate frame, we need the angle the surface normal makes on the sky light tangent plane $\varphi_{T_{\boldsymbol{\ell}}}$ and the angle it makes on the image plane φ_{Π}, respectively

$$\tilde{\boldsymbol{n}}_{T_{\boldsymbol{\ell}(\boldsymbol{x})}}(\boldsymbol{x}) = \boldsymbol{C}_{T_{\boldsymbol{\ell}(\boldsymbol{x})}} \boldsymbol{n}(\boldsymbol{x})\,, \tag{23}$$

$$\varphi_{T_{\boldsymbol{\ell}}}(\boldsymbol{x}) = \tan^{-1}\left(\frac{\tilde{\boldsymbol{n}}_{T_{\boldsymbol{\ell}(\boldsymbol{x})}}(\boldsymbol{x})_y}{\tilde{\boldsymbol{n}}_{T_{\boldsymbol{\ell}(\boldsymbol{x})}}(\boldsymbol{x})_x}\right) - \frac{\pi}{2}, \tag{24}$$

$$\varphi_{\Pi}(\boldsymbol{x}) = \cos^{-1} \boldsymbol{n}_{\Pi}(\boldsymbol{x})^{\mathsf{T}} \boldsymbol{y}_{\Pi}\,, \tag{25}$$

where $\boldsymbol{y}_{\Pi} = [0\ 1\ 0]^{\mathsf{T}}$ and $\tilde{\boldsymbol{n}}_{T_{\boldsymbol{\ell}(\boldsymbol{x})}}(\boldsymbol{x})$ is $\boldsymbol{n}(\boldsymbol{x})$ in the tangent plane coordinate frame.

Let us now derive each of the polarimetric reflection components of an object surface captured under the sun and sky. In the following, we drop pixel-dependency $\boldsymbol{x}$ from the notation for brevity.

Diffuse Reflection of Sky Theoretically speaking, we should integrate Eq. 18 in the upper hemisphere around the surface normal. This, however, would necessitate evaluation of the integral for each pixel in each step, causing an unnecessary computational burden since, especially after hemispherical integration, assuming uniform sky intensity would only cause 1% error in the diffuse reflection intensity. Instead, for diffuse reflection, unlike for specular reflection, we assume that the sky has uniform intensity, which significantly simplifies our model without sacrificing accuracy.

The diffuse reflection then becomes

$$\mathsf{S}^{d}_{\Pi} = \frac{\boldsymbol{C}(\varphi_{\Pi})}{2\pi} \boldsymbol{T}(\theta_{\Pi}) \int_{\Omega} (\boldsymbol{n}\cdot\boldsymbol{l}) \boldsymbol{D}(\zeta) \boldsymbol{T}(\theta_{\boldsymbol{l}}) \boldsymbol{C}(-\varphi_{\boldsymbol{l}}) \mathsf{S}_{\boldsymbol{l}} d\omega\,. \tag{26}$$

The integral of Eq. 26 yields a non-zero value only in the first component due to the matrix $D(\zeta)$:

$$\mathsf{S}_\Pi^d = \boldsymbol{C}(\varphi_\Pi)\boldsymbol{T}(\theta_\Pi) \cdot 2 I_d \zeta_d \mathsf{S}_0 \,, \tag{27}$$

where $\mathsf{S}_0 = [1, 0, 0, 0]^\top$, I_d is the uniform intensity of the sky, and ζ_d is a positive scalar value depending on the distribution of $\mathsf{S}_{\boldsymbol{l}}$. Note that ζ_d represents the "effective" diffuse albedo including the effects of depolarization by ζ and preceding and following transmittance. We thus recover ζ_d as the diffuse albedo. Here we assume that the $(1, 2)$ component of $T(\theta_{\boldsymbol{l}})$ is sufficiently small when compared with its $(1, 1)$ component. In this case, the polarization of $\mathsf{S}_{\boldsymbol{l}}$ does not contribute to ζ_d. This physically means that it does not contribute to the DC component of light transmitted into the object subsurface.

As a result, ζ_d is represented by

$$\zeta_d = \zeta \int_\Omega (\boldsymbol{n} \cdot \boldsymbol{l}) T_+(\theta_{\boldsymbol{l}}) d\omega \,, \tag{28}$$

and depends only on ζ and μ.

Diffuse Reflection of Sun The sun is unpolarized

$$\mathsf{S}_{\boldsymbol{s}} = 2 E_{\boldsymbol{s}} \delta(\boldsymbol{l} - \boldsymbol{s}) \mathsf{S}_0 \,, \tag{29}$$

where $E_{\boldsymbol{s}}$ is the sunlight irradiance. When the upper hemisphere around the surface normal includes the sun $\boldsymbol{s}$, polarization by diffuse reflection of the sun thus becomes

$$\mathsf{S}_\Pi^* = 2(\boldsymbol{n} \cdot \boldsymbol{s}) \zeta_d T_+(\theta_{\boldsymbol{s}}) I_{\boldsymbol{s}} \boldsymbol{C}(\varphi_\Pi) \boldsymbol{T}(\theta_\Pi) \mathsf{S}_0 \,, \tag{30}$$

where $\theta_{\boldsymbol{s}}$ is the angle between the sun and the surface normal, and $I_{\boldsymbol{s}}$ is

$$I_{\boldsymbol{s}} = \frac{E_{\boldsymbol{s}}}{\int_\Omega (\boldsymbol{n} \cdot \boldsymbol{l}) T_+(\theta_{\boldsymbol{l}}) d\omega} \,. \tag{31}$$

Specular Reflection of Sky We assume that, except for the sun, the specular reflection S_Π^s consists of mirror reflection of the sky. In this paper, specular reflection of the sun is ignored as it is a single saturated point with unreliable Stokes vector. We can simply fill this point's surface normal with surrounding estimates. For a given surface normal, we can compute the mirrored sky direction (Eq. 21), whose specular reflection can be computed as a Stokes vector using Eq. 4.

The reflected light then would be the total of diffuse reflection of the sky and sun and also specular reflection of the sky

$$\begin{aligned} \mathsf{S}_\Pi &= \mathsf{S}_\Pi^d + \mathsf{S}_\Pi^* + \mathsf{S}_\Pi^s \\ &= 2(I_d + (\boldsymbol{n} \cdot \boldsymbol{s}) I_{\boldsymbol{s}} T_+(\theta_{\boldsymbol{s}})) \zeta_d \boldsymbol{C}(\varphi_\Pi) \boldsymbol{T}(\theta_\Pi) \mathsf{S}_0 \\ &\quad + \zeta_s (\boldsymbol{n}^\top \boldsymbol{\ell}) \boldsymbol{C}(\varphi_\Pi) \boldsymbol{R}(\theta_\Pi) \boldsymbol{C}(-\varphi_{\boldsymbol{\ell}}) \mathsf{S}_{\boldsymbol{\ell}} \,, \end{aligned} \tag{32}$$

where ζ_s is the specular albedo.

5.2. Surface Normal Recovery

Given the generative model of observed polarization S_Π for a given surface normal $\boldsymbol{n}(\boldsymbol{x})$ (Eq. 32), our goal is to estimate the surface normal $\boldsymbol{n}$ for each pixel from as few as a single observation of the object captured under the sky.

Let us first assume that we know the sun direction $\mathbf{s}$, maximum degree of polarization of the sky $\rho_{\max}$, refractive index μ, the parameters of Perez sky model a, b, c, d, e, and sky zenith direction $\boldsymbol{g}$. The unknowns in Eq. 32 are then the intensity I_d, $I_{\boldsymbol{s}}$, $I_{\boldsymbol{\ell}(\boldsymbol{x}_0)}$ in $\mathsf{S}_{\boldsymbol{\ell}}$, albedo values ζ_s and ζ_d, and surface normal $\boldsymbol{n}$.

If we assume that the object surface consists of homogeneous material, only the surface normal $\boldsymbol{n}(\boldsymbol{x})$ will depend on pixel $\boldsymbol{x}$ in Eq. 32 and the other unknowns I_d, $I_{\boldsymbol{s}}$, $I_{\boldsymbol{\ell}(\boldsymbol{x}_0)}$, ζ_d, and ζ_s will be shared among all pixels. To further reduce the number of parameters, we can define I_{ζ_s} as $I_{\zeta_s} = I_{\boldsymbol{\ell}(\boldsymbol{x}_0)} \zeta_s$ without loss of generality. At the end, N pixel observations will have $3 + 2N$ degrees of freedom and $3N$ constraints when $\boldsymbol{n}(\boldsymbol{x})$ is unique to the observed Stokes vectors $\mathsf{S}_\Pi(\boldsymbol{x})$. In addition, polarimetric object appearance with N pixels captured from the same viewpoint but at M different times of the day will have $2M + 2N + 1$ degrees of freedom and $3M \times N$ constraints. As we can safely assume $N \gg M$, this suggests that, given a few images of the same object taken at different time instances (*i.e.*, changing solar direction) we can robustly estimate the object geometry.

We achieve this by alternating between estimating the pixel-shared parameters from a few pixels and then using those values to estimate the per-pixel parameters including the surface normals and albedo values. Assuming $I_s = t I_d$ with a constant t for all the M images, unknowns I_d, t, ζ_d and I_{ζ_s} are obtained by minimizing an L_2 Stokes error with the observed Stokes vector $\hat{\mathsf{S}}_\Pi$ as

$$\underset{I_d, t, \zeta_d, I_{\zeta_s}}{\arg\min} \sqrt{\textstyle\sum_{\boldsymbol{x}}^N \sum_i^M ||\hat{\mathsf{S}}_\Pi - \mathsf{S}_\Pi||^2} \,. \tag{33}$$

Using these estimates, we then estimate the surface normals

$$\underset{\boldsymbol{n}}{\arg\min} \sqrt{\textstyle\sum_i^M ||\hat{\mathsf{S}}_\Pi - \mathsf{S}_\Pi||^2} \,. \tag{34}$$

These two steps are iterated until convergence.

For the homogeneous material case with known sun direction, we can recover per-pixel surface normals from a single polarimetric image $M = 1$. In this case, we have $3 + 2N$ unknowns and $3N$ equations and the same alternating minimization algorithm can be used.

When assuming homogeneous material, even when we only have one polarimetric observation, we can further relax the requirement of known sky parameters: solar and sky zenith directions and Perez sky model parameters since, in general, the problem is well-conditioned ($N > 3$). The losses (Eq. 33 and Eq. 34) are, however, non-convex. To

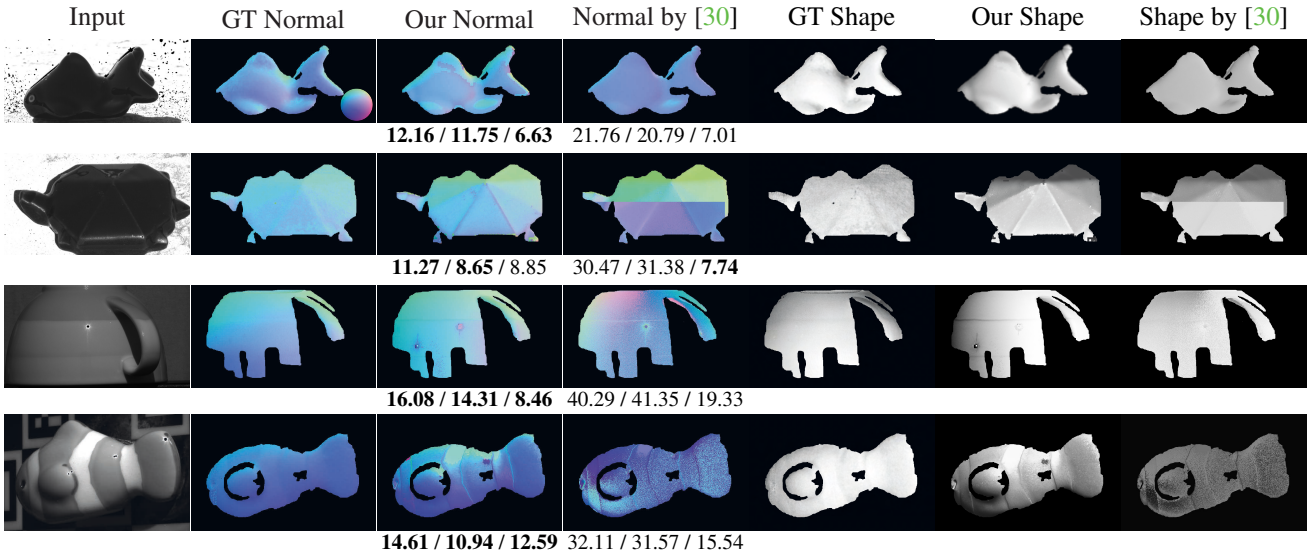

Figure 3: Quantitative results. Polarimetric input images were captured with an on-chip polarization camera. See color wheel in first row GT normal for normal directions. Quantitative analysis is shown with the three numbers under each surface normal map representing mean, median, and standard deviation of the angular errors from ground truth in degrees. Our method achieves quantitatively and qualitatively accurate geometry reconstructions of real objects with both homogeneous and spatially varying materials.

avoid local minima, we manually initialize these two directions (*e.g.*, by specifying the brightest point as the reflection of sun) and let the alternating minimization also estimate them as part of the pixel-shared parameters.

Finally, we can solve for texture, *i.e.*, spatially varying diffuse albedo $\zeta_d(\boldsymbol{x})$, for the general case of unknown sun and sky parameters. Object surfaces are often coated with the same material but can have underlying texture. In this case, for M images of an object surface occupying N pixels, we have $2M + 3N$ parameters for $3M \times N$ equations, and thus multiple polarimetric observations become essential. The required minimum number of observations at different times of the day are, however, just two ($\frac{3N}{3N-2} < M$ holds for any positive integer M larger than 1 for $N > 2$). We typically use 2 or 3 polarimetric images captured one or two hours apart in our experiments.

6. Experimental Results

We experimentally evaluate the effectiveness of our method with a number of real objects of different materials. We captured polarimetric images of these objects under a clear sky using a monochrome polarization camera with four on-pixel polarization filters of different angles (LUCID PHX050S-P) or a color digital SLR with a rotated polarization filter in front of the lens. For each image, we compute the Stokes vector at each pixel from these angular polarimetric observations. For some experiments, we captured the same object from the same viewpoint at different times of the day (*i.e.*, different sun directions).

The ground truth sun direction was computed by capturing a chrome sphere with the target, and the Perez sky parameters were set to represent the CIE standard clear sky [21]. The ground truth shape and normal of the target objects were computed by photometric stereo and structured lighting in a separate imaging session indoors.

Quantitative Evaluation We applied our method to real objects with different material compositions, including homogeneous and spatially varying diffuse albedo as well as different combinations of specular and diffuse reflection. Figure 3 shows the estimated surface normals and depths. Reconstructions are shown for surface regions reflecting the sky with manually specified masks. The overall shapes are visualized with shaded renderings of surfaces computed by integrating the normal maps for qualitative evaluation. We also show results of applying the method by Tozza *et al*. [30] to the same input images, which were computed with the code disseminated by the authors. Note that we chose this shape-from-polarization method as a baseline for comparison, but to our knowledge our method is the first to recover shape from sky polarization, so additional SOTA comparisons are not possible. The three errors for each normal estimate are the mean, median, and standard deviation of the angular errors between the ground truth in degrees. For these experiments, we used ground truth sun and sky parameters. For the first two objects, we further assumed homogeneous diffuse albedo. For each object, we used up to 3 polarimetric images (black fish: 1, turtle, cup: 2, and clownfish: 3) captured at different times of the day (*e.g.*,

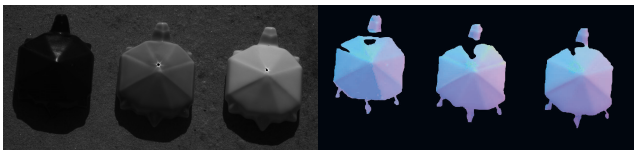

Figure 4: Grayscale images and reconstructions of objects of the same shape with different diffuse albedo corresponding to diffuse-dominant, mixed, and specular-dominant polarization from left to right, respectively. The mean/median/standard deviation of the normal errors in degrees are 14.69/14.44/6.10, 16.38/16.22/5.72, and 14.48/14.49/5.28, respectively. These results demonstrate the robustness of our method to different combinations of diffuse and specular reflection magnitudes.

2 hours apart). The results show quantitatively and qualitatively that our method can recover accurate fine geometry, except for areas that suffer from cast shadows or saturation by sun light, and significantly outperforms the baseline method. Even from a single polarimetric observation, we are able to reconstruct the complex shape for the black fish, and only up to 3 images are necessary to reconstruct fine geometry of texture objects (*e.g.*, clownfish). For the clownfish, the estimated normals have larger errors in the top center of the image. These errors are caused by insufficient separation in time between the input images.

Effect of Larger Diffuse Magnitude We also quantitatively evaluate the effect of varying magnitudes of diffuse reflection. Although our method can handle arbitrary combinations of diffuse and specular albedo at each pixel, as diffuse reflection is depolarized in the subsurface and its transmittance polarization is perpendicular to that of specular reflection, stronger diffuse reflection would retain less of the unique sky polarization pattern. As a result, surface normal estimation becomes more challenging as diffuse reflection becomes more dominant in magnitude (*e.g.*, white surfaces). Figure 4 shows reconstructions of three objects of the same shape (turtle) but in different colors, *i.e.*, black, green, and white, each representing predominantly specular, mixed, and diffuse object surfaces, respectively. The results show, both quantitatively and qualitatively, that our method is robust to changes in diffuse and specular relative magnitudes. These results demonstrate that our method can robustly handle a wide range of materials.

Fig. 1 and Fig. 5 show reconstruction results of different objects made of various materials ranging from natural to man-made, and strong diffuse to predominantly specular. Polarimetric input images were captured with either an on-chip polarization camera or a DLSR with a hand-rotated filter. The results show that our method can achieve fine geometry recovery for various types of real objects.

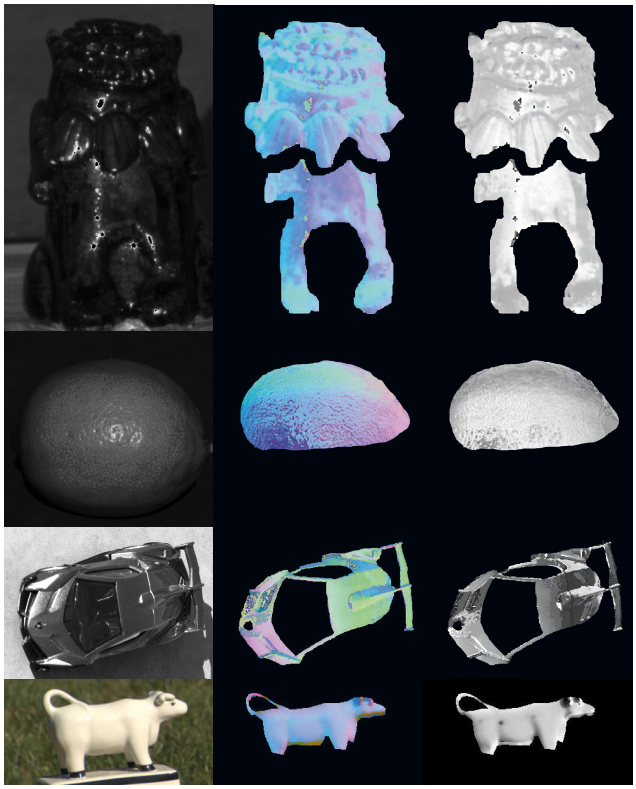

Figure 5: Reconstructed geometry of other real objects of complex materials and shapes. Reconstructions are shown for surface regions reflecting the sky with manually specified masks.

7. Conclusion

In this paper, we introduced a novel method for recovering surface normals from polarimetric images captured under the sky. Our method estimates the surface normal at each pixel by decoding the unique polarization pattern of the sky from its surface reflection. We demonstrated its effectiveness on a number of objects with different material compositions and showed that it can recover accurate fine geometry of a complex object even from a single polarimetric image. Especially with the advent of quad-Bayer polarization cameras, our method provides a simple and easy, completely passive tool for outdoor 3D sensing that would likely benefit a wide range of application domains.

Acknowledgement This work was in part supported by JSPS KAKENHI 17K20143, 18K19815, 20H05951, JST JPMJCR20G7, and NSF 1715195.

References

[1] Gary A Atkinson and Edwin R Hancock. Recovery of surface orientation from diffuse polarization. *IEEE transactions*

on image processing, 15(6):1653–1664, 2006. 2

[2] Seung-Hwan Baek, Daniel S Jeon, Xin Tong, and Min H Kim. Simultaneous acquisition of polarimetric svbrdf and normals. *ACM Trans. Graph.*, 37(6):268–1, 2018. 2, 4

[3] Edward Collett. The description of polarization in classical physics. *American Journal of Physics*, 36(8):713–725, 1968. 3

[4] Zhaopeng Cui, Jinwei Gu, Boxin Shi, Ping Tan, and Jan Kautz. Polarimetric multi-view stereo. In *Proceedings of the IEEE conference on computer vision and pattern recognition*, pages 1558–1567, 2017. 2

[5] Oana G Cula, Kristin J Dana, Dinesh K Pai, and Dongsheng Wang. Polarization multiplexing and demultiplexing for appearance-based modeling. *IEEE transactions on pattern analysis and machine intelligence*, 29(2):362–367, 2007. 2

[6] Graham Fyffe and Paul Debevec. Single-shot reflectance measurement from polarized color gradient illumination. In *2015 IEEE International Conference on Computational Photography (ICCP)*, pages 1–10, 2015. 2

[7] József Gál, Gábor Horváth, and Viktor Benno Meyer-Rochow. Measurement of the reflection–polarization pattern of the flat water surface under a clear sky at sunset. *Remote Sensing of Environment*, 76(1):103–111, 2001. 2

[8] Abhijeet Ghosh, Graham Fyffe, Borom Tunwattanapong, Jay Busch, Xueming Yu, and Paul Debevec. Multiview face capture using polarized spherical gradient illumination. In *Proceedings of the 2011 SIGGRAPH Asia Conference*, pages 1–10, 2011. 2

[9] Dennis H. Goldstein. Polarized light. 3rd, 2011. 2

[10] Giuseppe Claudio Guarnera, Pieter Peers, Paul Debevec, and Abhijeet Ghosh. Estimating surface normals from spherical stokes reflectance fields. In *European Conference on Computer Vision*, pages 340–349. Springer, 2012. 2

[11] Eugene Hecht. *Optics*. Addison Wesley, 4 edition, 2002. 3

[12] Stanley Heinze. *Polarization Vision*, pages 1–30. 01 2014. 2

[13] Stanley Heinze and Steven M Reppert. Sun compass integration of skylight cues in migratory monarch butterflies. *Neuron*, 69(2):345–358, 2011. 2

[14] Gábor Horváth and Dezsö Varjú. Polarization pattern of freshwater habitats recorded by video polarimetry in red, green and blue spectral ranges and its relevance for water detection by aquatic insects. *Journal of Experimental Biology*, 200(7):1155–1163, 1997. 2

[15] Achuta Kadambi, Vage Taamazyan, Boxin Shi, and Ramesh Raskar. Polarized 3d: High-quality depth sensing with polarization cues. In *Proceedings of the IEEE International Conference on Computer Vision*, pages 3370–3378, 2015. 2

[16] Wan-Chun Ma, Tim Hawkins, Pieter Peers, Charles-Felix Chabert, Malte Weiss, and Paul E Debevec. Rapid acquisition of specular and diffuse normal maps from polarized spherical gradient illumination. *Rendering Techniques*, 2007(9):10, 2007. 2

[17] Christine Merlin, Stanley Heinze, and Steven M Reppert. Unraveling navigational strategies in migratory insects. *Current opinion in neurobiology*, 22(2):353–361, 2012. 2

[18] Daisuke Miyazaki, Robby T Tan, Kenji Hara, and Katsushi Ikeuchi. Polarization-based inverse rendering from a single view. In *null*, page 982. IEEE, 2003. 2

[19] Olivier Morel, Fabrice Meriaudeau, Christophe Stolz, and Patrick Gorria. Polarization imaging applied to 3d reconstruction of specular metallic surfaces. In *Machine Vision Applications in Industrial Inspection XIII*, volume 5679, pages 178–186. International Society for Optics and Photonics, 2005. 2

[20] Trung Ngo Thanh, Hajime Nagahara, and Rin-ichiro Taniguchi. Shape and light directions from shading and polarization. In *Proceedings of the IEEE conference on computer vision and pattern recognition*, pages 2310–2318, 2015. 2

[21] International Commission on Illumination. *Spatial distribution of daylight - luminance distributions of various reference skies*. CIE technical report. CIE Central Bureau, 1994. 7

[22] Richard Perez, Robert Seals, and Joseph Michalsky. All-weather model for sky luminance distribution—preliminary configuration and validation. *Solar Energy*, 50(3):235 – 245, 1993. 5

[23] Stefan Rahmann and Nikos Canterakis. Reconstruction of specular surfaces using polarization imaging. In *Proceedings of the 2001 IEEE Computer Society Conference on Computer Vision and Pattern Recognition. CVPR 2001*, volume 1, pages I–I. IEEE, 2001. 2

[24] Jérémy Riviere, Ilya Reshetouski, Luka Filipi, and Abhijeet Ghosh. Polarization imaging reflectometry in the wild. *ACM Transactions on Graphics (TOG)*, 36(6):1–14, 2017. 2

[25] Soumyadip Sengupta, Hao Zhou, Walter Forkel, Ronen Basri, Tom Goldstein, and David Jacobs. Solving uncalibrated photometric stereo using fewer images by jointly optimizing low-rank matrix completion and integrability. *Journal of Mathematical Imaging and Vision*, 60(4):563–575, 2018. 2

[26] William A. P. Smith, Ravi Ramamoorthi, and Silvia Tozza. Linear depth estimation from an uncalibrated, monocular polarisation image. In *European Conference on Computer Vision*, pages 109–125. Springer, 2016. 2

[27] John William Strutt. Lviii. on the scattering of light by small particles. *The London, Edinburgh, and Dublin Philosophical Magazine and Journal of Science*, 41(275):447–454, 1871. 2

[28] John William Strutt. XV. on the light from the sky, its polarization and colour. *The London, Edinburgh, and Dublin Philosophical Magazine and Journal of Science*, 41(271):107–120, 1871. 2, 4

[29] Vage Taamazyan, Achuta Kadambi, and Ramesh Raskar. Shape from mixed polarization. *arXiv preprint arXiv:1605.02066*, 2016. 2

[30] Silvia Tozza, William AP Smith, Dizhong Zhu, Ravi Ramamoorthi, and Edwin R Hancock. Linear differential constraints for photo-polarimetric height estimation. In *Proceedings of the IEEE International Conference on Computer Vision*, pages 2279–2287, 2017. 2, 7

[31] Rüdiger Wehner. Polarization vision–a uniform sensory capacity? *Journal of Experimental Biology*, 204(14):2589–2596, 2001. 2

[32] Rüdiger Wehner and Thomas Labhart. Polarization vision. *Invertebrate vision*, 291:348, 2006. 2

[33] Jinyu Zhao, Yusuke Monno, and Masatoshi Okutomi. Polarimetric multi-view inverse rendering. In *European Conference on Computer Vision*, pages 85–102, 2020. 2

[34] Dizhong Zhu and William AP Smith. Depth from a polarisation+ rgb stereo pair. In *Proceedings of the IEEE Conference on Computer Vision and Pattern Recognition*, pages 7586–7595, 2019. 2